

ARTICLE OPEN



Tailoring phonon modes of few-layered MoS₂ by in-plane electric field

Sreemanta Mitra^{1,2}, Divya Srivastava^{3,4,8}, Shib Shankar Singha^{1,5,8}, Saurav Dutta⁶, Biswarup Satpati⁷, Maarit Karpinen³, Arindam Ghosh² and Achintya Singha¹

We discuss the effect of the in-plane electric field on the Raman spectroscopy for few-layered MoS₂. The characteristic Raman modes of MoS₂ show gradual red shift, while the intensity increases by 45–50% as the electric field is increased, showing a large electro-optical effect. Structural analysis suggests that our few-layered MoS₂ belongs to P6/m2 space group with broken inversion symmetry. We attribute this gradual red shift to this broken symmetry-driven piezoelectricity in MoS₂, which generates tensile strain along the perpendicular direction when the electric field is applied. The enhancement of the effect upon reversing the electric field direction adds credence to our interpretation. Our first principal density-functional theory calculation further substantiates the claim. This optical probing of the electromechanical coupling may lead to applications as a nonextensive technique for electric field/strain sensors in the nanoelectronics devices.

npj 2D Materials and Applications (2020)4:6; <https://doi.org/10.1038/s41699-020-0138-y>

INTRODUCTION

Tunability of two-dimensional quantum materials (2DQM) through an external perturbation has strongly excited condensed matter research in recent years due to its possibility of applications, if not by the rich physics they offer¹. Graphene and other 2DQMs^{2–6} exhibit a wealth of unusual and fascinating properties, such as Dirac² or Weyl semimetal, topological insulator^{7,8}, charge-density wave⁹, and superconductivity^{7,10}. Among the vast library of 2DQM⁶, atomically thin semiconducting transition metal dichalcogenides (TMDCs) (having formula MX₂, M = Mo and W and X = S, Se, and Te) have attracted particular interest in optoelectronic application due to their strong light–matter interaction owing to the presence of van-Hove singularity in their electronic structure^{11,12}. The bulk 3D TMDCs are formed by the stacking of individual layers through a weak van der Waal's (vdW) force, making them easy to cleave and get a monolayer, whereas the atoms within each 2D plane are bound through a strong covalent bonding¹². Thus, the huge difference between in-plane and out-of-plane interatomic interaction strengths often results in highly anisotropic electronic and mechanical properties in these layered systems. Coupling of these anisotropic properties may lead to interesting phenomena.

Quasi-2D molybdenum disulfide (MoS₂)¹³ is a prototype material to study the light–matter interaction, since it has shown promising optoelectronic applications¹⁴. MoS₂ crystallizes in hexagonal structure and belongs to the space group/point group P3m1/D_{6h} (with inversion symmetry). Similar to other vdW crystals, e.g., graphene, an atomically thin version of this naturally occurring MoS₂ has been successfully obtained by mechanical exfoliation^{13–15} or liquid-phase exfoliation¹⁶. The anisotropic crystal structure, strong in-plane Coulomb interaction, and weak out-of-plane van der Waal's interaction of MoS₂ leads to several interesting anisotropic optical and electronic behavior^{17–22}. Both

monolayer and few-layered MoS₂ exhibit a number of intriguing physical properties, including a direct optical bandgap of about 1.8 eV^{13,14}, strong photoluminescence (PL), electroluminescence^{13,14,23,24}, and reasonably high mobility of the order of 0.2 m²/Vs^{25,26}. Numerous studies indicate that monolayer MoS₂ exhibits large exciton- and trion-binding energies²⁷, inversion symmetry breaking together with strong spin–orbit coupling²⁸, and valley Hall effect²⁹. These indicate the promising possibility of MoS₂ in next-generation nanoelectronics^{15,30} and photonics³¹ applications.

Raman spectroscopy, a powerful tool to probe the phonons in solids, has been used extensively as a nondestructive method to characterize electronic and vibrational properties of 2DQMs^{32,33}. It has also been used for identification of a number of layers^{33–35}, and the twist angle between the layers in 2DMs³⁶. MoS₂ shows two distinct and well-defined types of Raman modes, one due to the stretching of S atoms along the *c* axis (A mode) and the other is from the in-plane breathing motion (E_{2g}¹ mode)^{12,20,33,37}. The resonance excitation (~1.8–2.0 eV) gives rise to a rich spectrum of second-order peaks and multiphonon bands^{26,33} due to strong electron–phonon coupling, and is widely used as the fingerprint characterization of MoS₂³³. However, the effect of external perturbation on the Raman spectrum of MoS₂ is not extensively reported. Although recently, a giant increase in the phonon modes' intensity has been observed in monolayer to bulk MoS₂ under a magnetic field³⁷ and electron irradiation³⁸, the effect of the electric field (E) is still unknown. Recently, the gate voltage dependence on the optical properties in general, has been discussed for MoS₂, along with its possibility as optical modulators³⁹. The effect of the gate voltage on the Raman spectroscopy has also been discussed³⁹.

In this paper, we describe the effect of moderate in-plane electric field on the phonon modes of few-layered MoS₂, probed by Raman spectroscopy at room temperature. We have been able

¹Department of Physics, Bose Institute, Kolkata 700009, India. ²Department of Physics, Indian Institute of Science, Bangalore 560012, India. ³Department of Chemistry and Materials Science, Aalto University, FI-00076 Aalto, Finland. ⁴Department of Physics, Central University of Rajasthan, Ajmer 305817 Rajasthan, India. ⁵Department of Physics, Brahmananda Keshab Chandra College, Kolkata 700108, India. ⁶Department of Physics, Rammohan College, Kolkata 700009, India. ⁷Surface Physics and Material Science Division, Saha Institute of Nuclear Physics, Kolkata 700064, India. ⁸These authors contributed equally: Divya Srivastava, Shib Shankar Singha. [✉]email: sreemanta85@gmail.com; achintya@jcbosc.ac.in

to correlate the effect of the applied electric field to the strain generated in MoS₂, by density-functional theory (DFT)-based first-principal calculations of its phonon modes.

RESULTS

Structural characterization

The morphology of the as-prepared MoS₂ was observed in transmission electron microscopy (TEM) and shown in Fig. 1a. It possesses nanosheet-like structure. In the inset of Fig. 1a we show the thickness map by Energy Filter TEM imaging recorded at 300 keV. The higher magnification image of the yellow-colored highlighted area in Fig. 1a is shown in Fig. 1b. We calculate the interplanar spacing as 0.63 nm, which corresponds to (002) plane of MoS₂ from the high-resolution TEM image (Fig. 1b). The selected area electron diffraction (inset of Fig. 1b) shows the hexagonal lattice arrangement of MoS₂. The line profile along the blue rectangular box (Fig. 1a, inset) gives a numerical value of the relative thickness (t/λ_x) of the specimen (Fig. 1c), where t is the thickness and λ_x is inelastic mean-free path of the electron^{40,41}. The thickness of the material can be determined by knowing λ_x , which is 119 nm⁴⁰ at 300 keV. This implies that the average thickness of one of the segments of the MoS₂ flake (highlighted in Fig. 1a, inset) is ≈ 1.8 nm, which is close to the thickness of a three-layered MoS₂. A typical thickness distribution histogram,

measured in a similar manner, is shown in Fig. 1d. The crystalline structure and phase of MoS₂ nanosheets were further confirmed by XRD as shown in Fig. 1e, with the respective lattice planes shown in parenthesis^{42,43}. In Fig. 1e, the dots represent the experimental points, while the blue line is the Rietveld refinement fit^{44,45} and the red line is the difference between the two. The structural refinement suggests that our MoS₂ sample is of pure hexagonal structure (space group P63/mmc) with the lattice parameters $a = b = 0.3117$ nm and $c = 0.127$ nm. We observe a shrinkage along the a and b axes and an elongation along the c axis. Compared with the standard relative intensities of different peaks, it is found that (103) and (105) peaks are suppressed, indicating an irregular stacking arrangement of the atomic layers⁴⁶. Since ($h-k=0$) reflections are unaffected by the stacking fault broadening, the (110) reflection has a larger relative intensity than (103) and (105) peaks. Furthermore, it can be seen from the fitting parameters in Supplementary Table 1 (see supplementary information) that the fault probability is $\approx 14\%$, suggesting a disordered stacked system.

Raman spectra characterization of MoS₂

The Raman spectra of our few-layered MoS₂ at various in-plane electric fields are shown in Fig. 2. For zero field, the major characteristic Raman modes are observed at 382.5 and 406.7 cm⁻¹ that belong to the in-plane E_{2g} and out-of-plane A_{1g} vibrations,

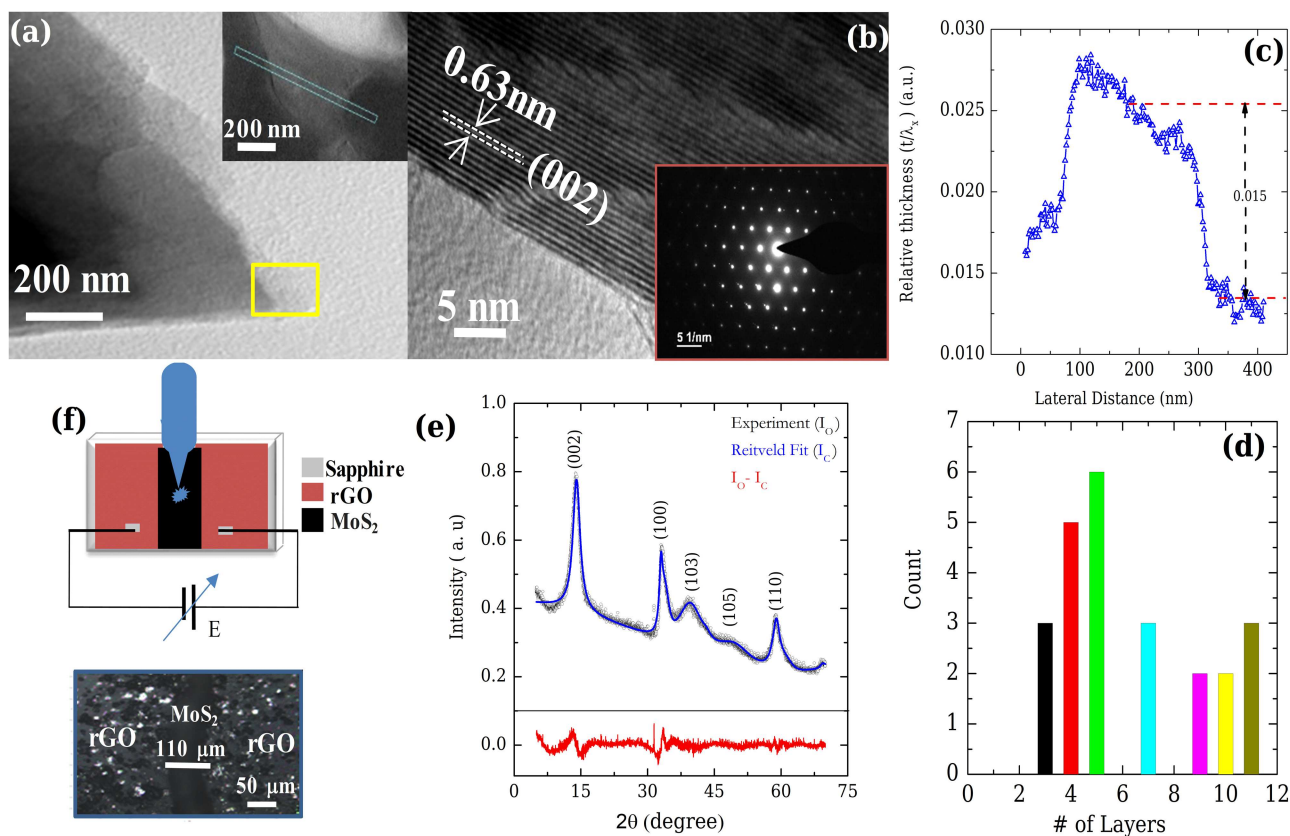


Fig. 1 Primary characterization and experimental setup. **a** Transmission electron micrograph of the prepared MoS₂. (Inset: Relative thickness map recorded at 300 keV by energy filter TEM imaging. The blue rectangular box on the image indicates the integration width.) **b** The high-resolution image, obtained from the yellow marked area in panel (a), showing the lattice planes. The interplanar distance is 0.63 nm, which corresponds to the (002) plane of MoS₂. (Inset) The selected area electron diffraction pattern of MoS₂ showing the hexagonal lattice arrangement. **c** The relative thickness profile of the MoS₂ flake as determined from the energy filter TEM image along the blue box marked in panel (a) inset. The thickness is obtained (for details, see the text) as ≈ 1.8 nm. **d** A histogram, showing the occurrence of different layers in the as-prepared MoS₂. **e** X-ray diffraction of the MoS₂ powder. The corresponding lattice planes are shown in parentheses. The blue solid line is the Rietveld fit to the experimental data. The red line is the difference between the experiment and the fit. The low value of the residue suggests a good fit. The Rietveld analysis suggests that the MoS₂ belongs to P6/m2 space group, with broken inversion symmetry. **f** The experimental arrangement and the optical micrograph of the device. The channel for MoS₂ is 110- μm wide. The Raman spectroscopy was performed on a flake in the middle of the channel.

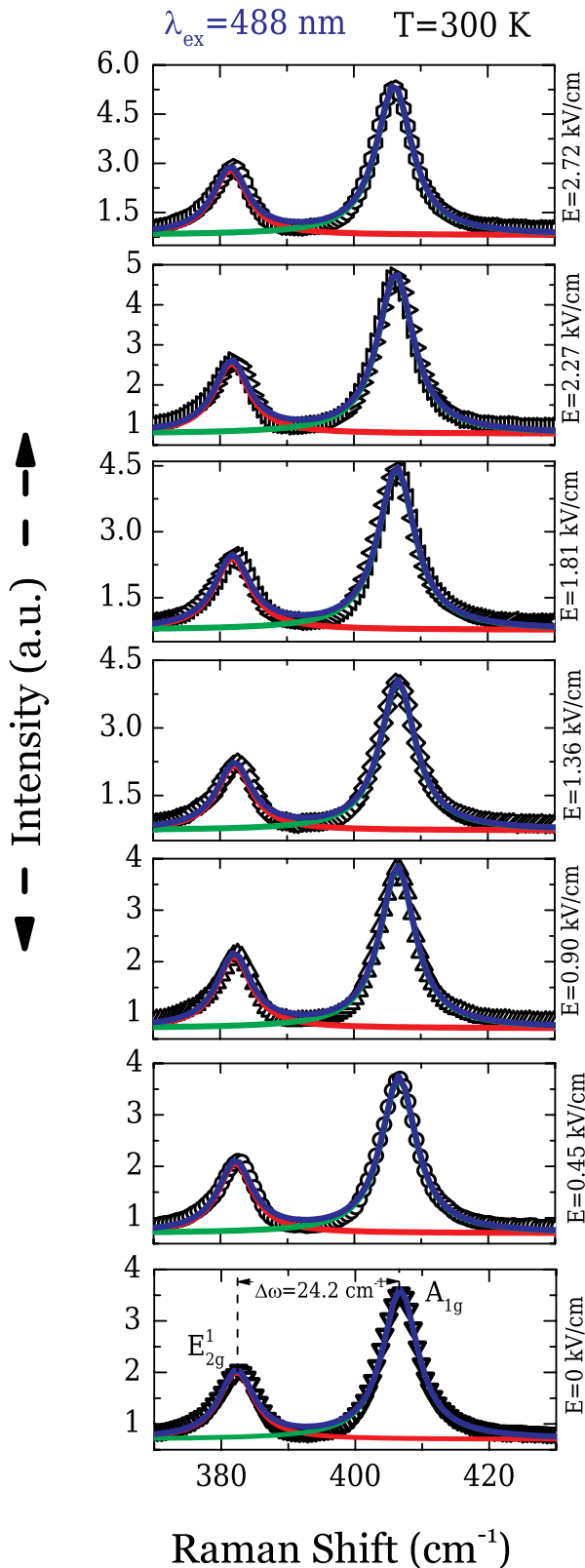


Fig. 2 Raman spectra of MoS₂ under different electric fields (E). The plots of the Raman spectra of few-layered MoS₂ under various in-plane electric fields, measured at room temperature. A blue laser of 488-nm wavelength has been used for the excitation. The solid lines are the damped harmonic oscillator (Lorentzian) model fit to the experimental data to identify multiple peaks. The E_{2g}¹ and A_{1g} peak respectively appears at 382.5 and 406.7 cm⁻¹ for zero field. The difference between the peak position is 24.2 cm⁻¹. Under the application of successive in-plane electric field, the position of E_{2g}¹ and A_{1g} shows gradual red shifts. The peak separation remains almost unaffected, whereas the intensity of the peaks increases with increasing the electric field (E).

what is observed earlier for the five-layered MoS₂^{34,35}. Furthermore, the presence of a strong direct PL (and subsequent absence of an indirect PL) (see supplementary information) suggests that our MoS₂ is indeed a few-layered thick, as the bulk MoS₂ shows only indirect electronic transition^{35,47}.

Electric field effect on Raman spectra of MoS₂

As the in-plane electric field is increased, both the Raman characteristic peaks showed gradual red shifts in frequency (Fig. 2). This can be seen more clearly in Fig. 3, where we show the (a) E_{2g}¹ and (b) A_{1g} spectra measured at different electric fields. A clear change in the peak position for both the peaks with the changing electric field can be observed. Alongside the shift in the peak positions to a lower value, the peak intensity increases with the increase in the electric field (Fig. 3d), while the full-width-half-maxima (FWHM) remain almost unchanged (Fig. 3c). Moreover, the difference between the E_{2g}¹ and A_{1g} peak remains almost unaffected over the window of the applied electric field (see supplementary information). The intensity of the phonon modes increased substantially by 45–50% as the electric field is increased (Fig. 3d), implying a large electro-optical coupling. This gradual increase can be attributed to the manipulation of the MoS₂ electrons under the electric field as it in turn affects the Raman phonon intensity³⁷. A more careful look at the Raman spectra reveals the presence of an asymmetry near 377 cm⁻¹^{48,49}, which appears due to the transverse optical phonon mode of MoS₂. The presence of this asymmetry in the zero electric field spectra allows us to infer that this arises due to the quality of the sample and is not related to the effect of the electric field.

DISCUSSION

The intriguing red shift of principal phonon modes of MoS₂ under the electric field, can be attributed to the doping by source–drain bias due to the electric field or by an increase in temperature due to Joule heating. The effect of temperature, in this case, can be refuted as under increasing temperature, the Raman peak intensity decreases and the FWHM increases⁵⁰, while we observe the opposite trend in our system. The electrostatic doping, due to band bending, on the other hand, can lead to the softening of the phonon modes. However, the moderate applied electric field, to our understanding, will not be able to induce doping in the few-layered MoS₂ under consideration.

On the contrary, we believe that the red shifts in Raman spectra under the electric field can be due to the strain generated in the system. MoS₂, with an even number of layers, belongs to the P3m1 space group and with an odd number of layers belongs to the P6m2 space group (without inversion symmetry)^{51,52}. Interestingly, this broken inversion symmetry induces piezoelectricity in MoS₂ with an odd number of layers^{51,52}. Notably, in a piezoelectric material, if an electric field is applied, a strain is generated along its perpendicular direction and vice versa. This piezoelectricity in MoS₂ develops and vanishes as the number of

respectively³⁵. As an indirect measure, the position and the difference between the E_{2g}¹ and A_{1g} evolves with the increase in the number of layers in MoS₂ until six layers before it gets saturated^{12,34,35}. At zero electric field, we find that the difference between these two Raman modes is 24.2 cm⁻¹, which is close to

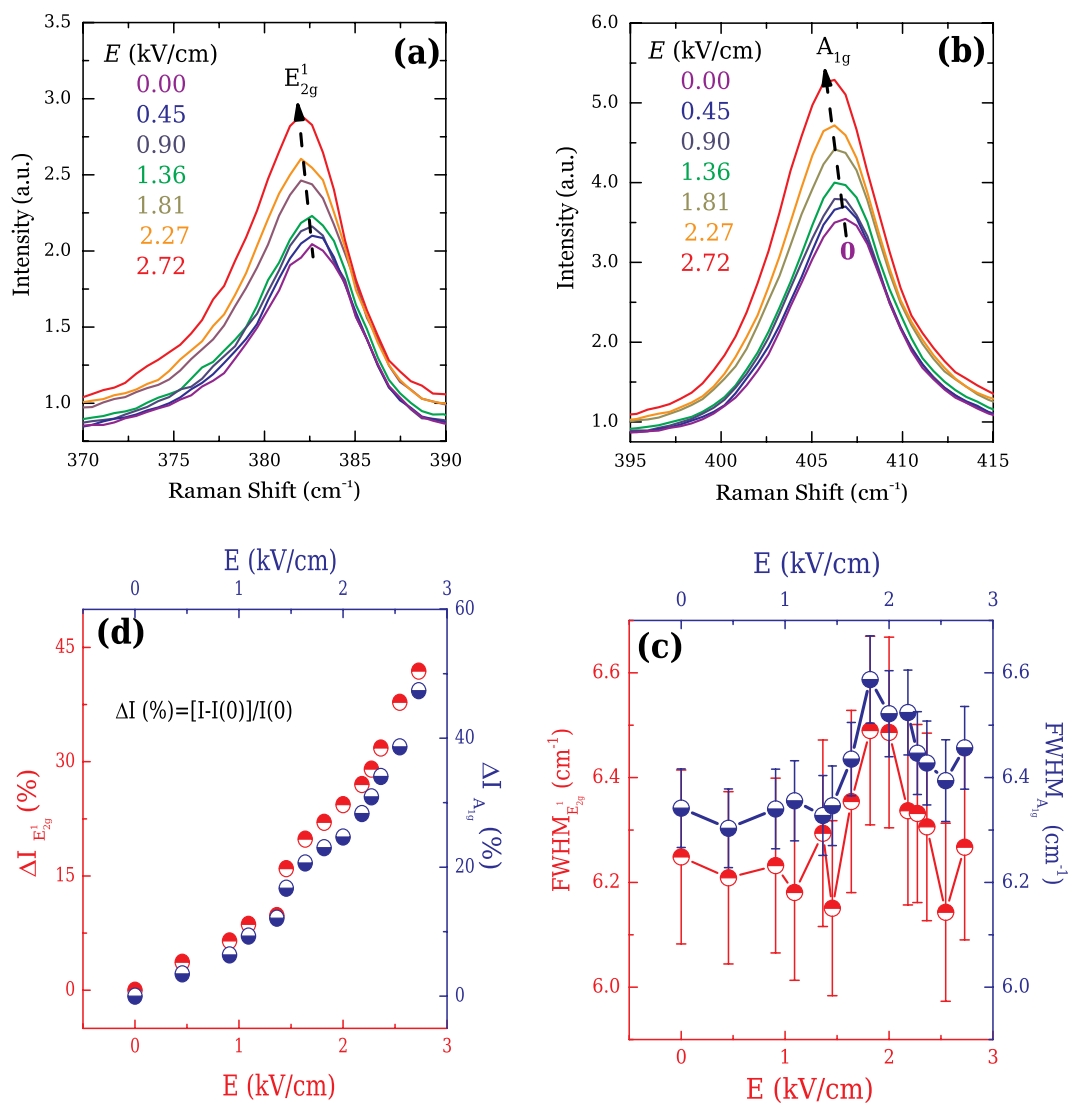


Fig. 3 Effect of the electric field (E) on the Raman modes of MoS_2 . Plots of the Raman spectra of **a** E_{2g}^1 and **b** A_{1g} mode under different in-plane electric fields for the few-layered MoS_2 . The electric field values are color-matched with the plots. The peak positions gradually shift to a lower wave number as the electric field is increased. **c** The Raman peaks' full-width half-maxima (FWHM) as obtained from the Lorentzian fit to the experimental data shown in Fig. 2. The FWHM for E_{2g}^1 (in red, left and bottom axis) and A_{1g} (in blue, right and top axis) stays fairly constant over the electric field window. The lines are to guide the eye. The error bars are obtained from the least-square fit of the experimental Raman spectroscopy data to the damped harmonic oscillator model (refer to Fig. 2). **d** The relative percentage change of the intensity (normalized with respect to the zero-field value) of E_{2g}^1 (in red, left and bottom axis) and A_{1g} (in blue, right and top axis) mode increases gradually as the electric field is increased. A substantial change of about 45–50% is observed for both the characteristic peaks in the measurement window, suggesting a strong electro-optical coupling.

layers change from odd to even due to the breaking and the recovery of the inversion symmetry^{51,52}. As our MoS_2 belongs to the space group $P6m2$, we believe that the applied in-plane electric field induces an out-of-plane tensile strain in it due to the broken inversion symmetry-driven piezoelectricity.

To substantiate our claim, we performed DFT-based first-principal calculations of the Raman active phonon modes of MoS_2 for different percentages of out-of-plane tensile strains on it (for calculation details, see “Methods” section).

The DFT-calculated, Raman active modes of MoS_2 , for zero tensile strain (or zero electric field) occur at 385.3 cm^{-1} (E_{2g}^1), and 408.3 cm^{-1} (A_{1g}), which is in agreement with the experimental results^{12,33,53}. The plots for the calculated Raman modes are shown in the supplementary information.

In Fig. 4a, b, we show the experimental change in the Raman mode for E_{2g}^1 and A_{1g} with the applied electric field, with respect

to its zero electric field value. In the same figure, we show the corresponding change in Raman frequency with applied out-of-plane tensile strain with respect to its zero-strain value, calculated by first-principal calculation. With the applied electric field/tensile strain, both the E_{2g}^1 and A_{1g} modes shift to lower frequencies. The frequency shift ($\Delta\omega$) is defined as the difference between the frequencies of Raman active mode E_{2g}^1 (A_{1g}) at a finite electric field/tensile strain and at zero electric field/tensile strain. Mathematically, $\Delta\omega_{ph} = \omega_{ph}(E) - \omega_{ph}(E = 0)$ where ‘ph’ stands for either E_{2g}^1 or A_{1g} . It is found that the frequencies of E_{2g}^1 and A_{1g} decrease with increasing tensile strain along [001] direction in a similar manner as it changes with the applied in-plane electric field. Our first-principal calculation results are in agreement with the experimental data within an acceptable limit, and show similar features as observed previously on DFT-based calculation of Raman modes of MoS_2 under tensile strain^{16,26}. The tensile strain

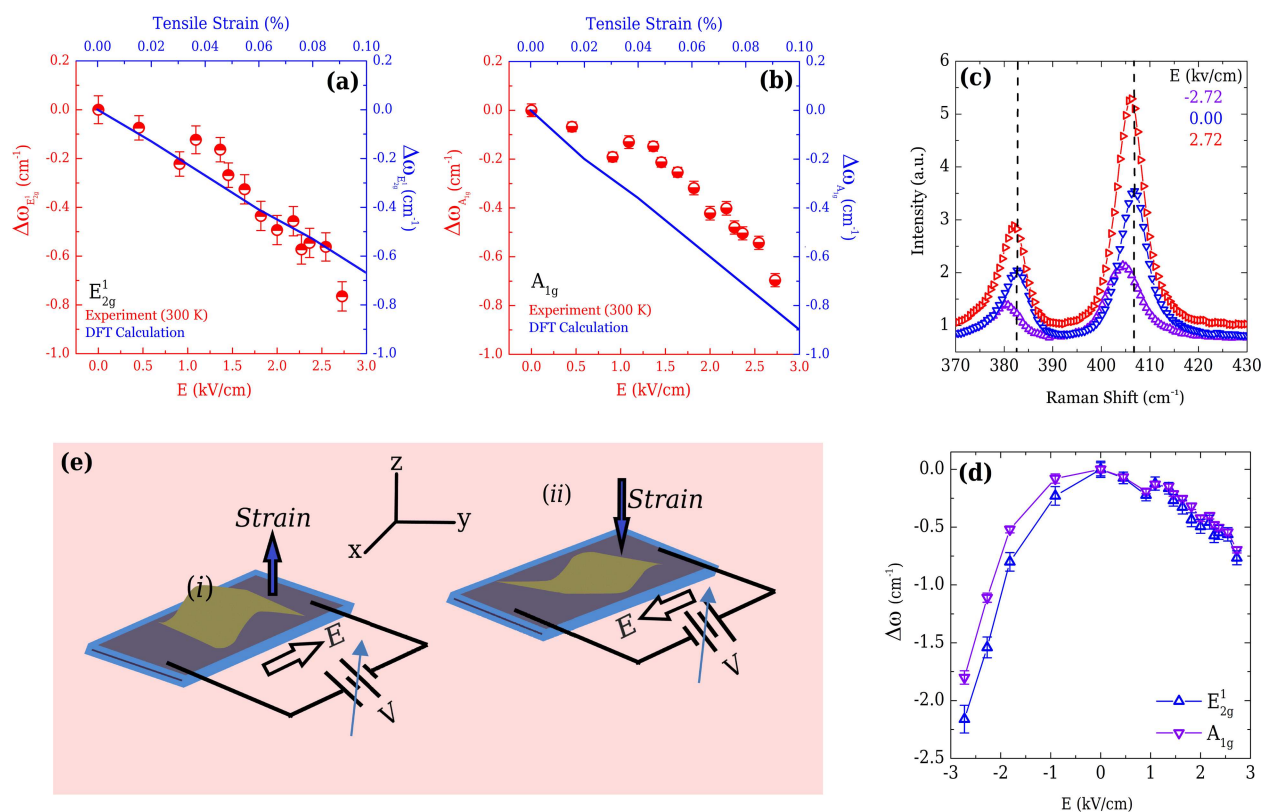


Fig. 4 Comparison of the successive shifts of the Raman modes under an electric field (tensile strain). The plots of the successive shift of Raman mode with respect to its zero-field (or zero-strain) value. The symbols are the experimental data (in red, left and bottom axis), and the solid line is the theoretical calculation (in blue, right and top axis). $\Delta\omega_{ph} = \omega_{ph}(E) - \omega_{ph}(E = 0)$ where ‘ph’ stands for either E_{2g}^1 or A_{1g} . The variation of experimental (red, left axis) and theoretical (blue, right axis) $\Delta\omega$ with the electric field (E) (red bottom axis) or tensile strain (blue, top axis) for **a** E_{2g}^1 and **b** A_{1g} modes. $\Delta\omega$ for both E_{2g}^1 and A_{1g} decreases linearly with the electric field or tensile strain. The errors in determining $\Delta\omega$ are obtained from the Lorentzian fit to the experimental data (see Fig. 2). **c** Raman spectra of few-layered MoS_2 under two different directions of the applied electric field along with the zero-field data. For both the directions of the applied electric field (E), the principal Raman modes show a red shift in frequency with respect to their zero-field value (indicated by black dashed lines). **d** The plots of the successive shift of Raman mode under different directions of the applied electric field with respect to their zero-field value. The lines are to guide the eye. **e** Cartoon describing the experimental situation for observance of a different amount of shifts of the phonon mode frequency by reversing the direction of the applied electric field. In case (i) the strain is applied along the free surface of MoS_2 flake, whereas for case (ii), it is toward the substrate. The substrate suppresses the effect of strain, leading to a lesser change in the Raman shifts under the electric field.

increases the interlayer distance between S–Mo–S layers, which weakens the vdW interactions between adjacent layers. This results in a red shift in both E_{2g}^1 and A_{1g} modes. However, for a given tensile strain, a reduction in Raman shift of the A_{1g} mode is larger than that of the E_{2g}^1 mode. In the A_{1g} mode (arises from out-of-plane vibration of S atoms in the opposite direction along the z direction), the change in atomic vibration is dominated by interlayer force. While for E_{2g}^1 long-range coulombic interlayer force plays a key role³⁴ and thus explains the observations.

Raman spectroscopy measurements by reversing the polarity of the electric field (Fig. 4c) add more credence to our claim of this electric field-controlled strain-mediated tailoring of the principal phonon modes of MoS_2 . Intuitively, we expect a similar outcome as before, and indeed observe similar red shifts of the phonon modes with respect to the electric field (Fig. 4c). However, the magnitude of the change in the phonon mode frequency under the electric field with respect to its zero-field value is different in two different directions of the electric fields (Fig. 4d). A simple diagrammatic approach (Fig. 4e) of the experimental situation can help us to understand this. Although it cannot be determined unambiguously, we consider that the left panel [(i) of Fig. 4e] denotes the negative electric field direction, whereas the right panel [(ii) in Fig. 4e] denotes the positive electric field direction in accordance with our previous analogy. For (i), the piezoelectric strain on the MoS_2 flake is along the out-of-plane (positive z)

direction; however, for (ii), it is along the negative z direction. Now for situation (i), the strain is applied along the free surface, leading to a larger change in the phonon mode frequency in contrast to situation (ii) where the strain is acting along a direction of the supporting substrate and thus is being suppressed. This leads to the difference in the magnitude of the change in the phonon mode frequency on either direction of the applied electric fields. We presume that this would be symmetrical about the zero field, if the flake is freely standing or supported by the identical surfaces on both sides, although, for the latter, the effect of pressure might also complicate the outcome. Interestingly, this behavior of different magnitude of the effect by reversing the polarity of the electric field can possibly exploit odd-layered MoS_2 in switching applications.

In summary, we prepared few-layered MoS_2 nanoflakes by a chemical bottom-up approach and performed Raman spectroscopic measurements under a moderate in-plane electric field. The Rietveld analysis of the X-ray diffraction suggests that the prepared MoS_2 is of hexagonal phase with broken inversion symmetry. Under the increasing in-plane electric field, both the prominent characteristic Raman modes of MoS_2 show gradual red shifts (in frequency), which we believe is due to the out-of-plane tensile strain generated due to the intrinsic piezoelectricity in MoS_2 with an odd number of layers. Our first-principal calculation of the Raman modes of MoS_2 under different percentages of out-

of-plane tensile strain shows a similar red shift and adds credence to our claim. Experimentally, our interpretation was further supported by the Raman spectroscopy measurements by reversing the polarity of the electric field. Such an optical probing of the electromechanical coupling may lead to diverse applications as a nonextensive technique for the electric field and (or) strain sensors in the nanoelectronic devices.

METHODS

Sample preparation

The MoS₂ samples were prepared by a chemical bottom-up approach by using molybdenic oxide and potassium thiocyanate as precursor materials. These were mixed in ≈1:5, in distilled water and stirred to get a homogeneous mixture. This was then transferred into a Teflon-lined stainless-steel autoclave and was heated at 493 K for 24 h. Following this, the mixture was brought back to room temperature, and the resultant precipitate was washed thoroughly by distilled water and collected using centrifugation at 4000 rpm. Finally, the sample was dried at 353 K for 6 h under N₂ gas flow to obtain the dark-gray MoS₂ powder.

Device fabrication

Reduced graphene oxide (rGO) was prepared by reducing GO (for details of preparation, see ref. ⁵⁴) and spin-coated on Sapphire substrate with a predefined mask. After rGO deposition, the mask was removed and a narrow channel (≈110 μm) was observed. The prepared MoS₂ was spin-coated on rGO/Sapphire substrate. The electrical connection was done by putting silver electrodes. A schematic diagram and optical image of a simple device are presented in Fig. 1f.

Experiments

X-ray diffraction (XRD) was performed using a Rigaku (MiniFlex II) diffraction instrument with CuK_α radiation. Transmission electron microscopy (TEM) was done in FEI TECNAI G2 F30. Raman and photoluminescence (PL) measurements were done using a micro Raman Spectrometer (LabRam HR, Jobin Yvon) equipped with Peltier cooled CCD detector (pixel size 1024 × 256) at room temperature. We used an Argon ion blue (488-nm) laser as an excitation source, and a ×50 objective was used to focus the laser beam on the sample. The slit width of the spectrometer is 100 μm and grating of line 1800/mm is used. The spectral resolution of the spectrometer is 0.35 cm⁻¹/pixel. The integration time for taking the Raman spectra was 30 s. The laser power was maintained at 0.2 mW throughout the measurement. A Keithley 2400 source meter was used to apply the electric field. The experimental arrangement has been shown as a schematic in Fig. 1f.

DFT calculation

The first-principal calculations have been carried out in GGA framework as implemented in QUANTUM ESPRESSO^{55–57}. The optimized lattice parameters are $a = b = 0.314$ and $c = 1.240$ nm, while the experimental lattice parameters are $a = b = 0.3117$ and $c = 1.27$ nm⁵⁸. The primitive lattice vectors of MoS₂ are $\vec{a} = (a, 0, 0)$, $\vec{b} = (a/2, \sqrt{3}a/2, 0)$, and $\vec{c} = (c, 0, 0)$. The tensile strain along the z direction is defined (%ε_z) as the ratio of elongation in the length of the c vector (Δc) to its original length ($\frac{\Delta c}{c} \times 100$). After applying the strain along the z direction, self-consistent calculations are performed on the geometry, and vibrational modes at the center (Γ) of Brillouin zone are calculated using density-functional perturbation theory. PBEsol⁵⁷ exchange and correlation functional is adopted with scalar-relativistic PAW pseudopotentials. This functional provides accurate phonon frequencies compared with experimental data⁵⁹. The plane-wave basis cutoff is taken to be 55 Ry. Brillouin-zone sampling has been done using Monkhorst–Pack-type k-point mesh of 23 × 23 × 23 for self-consistent calculations. The vdW interactions are treated via the semiempirical dispersion correction DFT-D2 proposed by Grimme⁶⁰. The lattice constants are obtained by performing the structural optimization until the total force on atoms was <0.0001 Ry/au.

DATA AVAILABILITY

The data that support the findings of this study are available from the corresponding author on reasonable request to S.M. (email: sreemanta85@gmail.com) or A.S. (email: achintya@jcbose.ac.in).

Received: 2 October 2019; Accepted: 28 February 2020;

Published online: 30 April 2020

REFERENCES

- Basov, D. N., Averitt, R. D. & Hsieh, D. Towards properties on demand in quantum materials. *Nat. Mater.* **16**, 1077 (2017).
- Novoselov, K. S. et al. Electric field effect in atomically thin carbon films. *Science* **306**, 666–669 (2004).
- Geim, A. K. & Novoselov, K. S. The rise of graphene. *Nat. Mat.* **6**, 183–191 (2007).
- Mas-Ballesté, R., Gómez-Navarro, C., Gómez-Herrero, J. & Zamora, F. 2D materials: to graphene and beyond. *Nanoscale* **3**, 20–30 (2011).
- Xu, M., Lian, T., Shi, M. & Chen, H. Graphene-like two-dimensional materials. *Chem. Rev.* **113**, 3766–3798 (2013).
- Butler, S. Z. et al. Progress, challenges, and opportunities in two-dimensional materials beyond graphene. *ACS Nano* **7**, 2898–2926 (2013).
- Fatemi, V. et al. Electrically tunable low-density superconductivity in a monolayer topological insulator. *Science* **362**, 926–929 (2018).
- Zhang, H. et al. Topological insulators in Bi₂Se₃, Bi₂Te₃ and Sb₂Te₃ with a single Dirac cone on the surface. *Nat. Phys.* **5**, 438–442 (2009).
- Wu, D. et al. Layered semiconductor EuTe₄ with charge density wave order in square tellurium sheets. *Phys. Rev. Materials* **3**, 024002 (2019).
- Sajadi, E. et al. Gate-induced superconductivity in a monolayer topological insulator. *Science* **362**, 922–925 (2018).
- Wilson, J. A. & Yoffe, A. D. The transition metal dichalcogenides discussion and interpretation of observed optical, electrical, and structural properties. *Adv. Phys.* **18**, 193–335 (2006).
- Zhang, X. et al. Phonon and Raman scattering of two-dimensional transition metal dichalcogenides from monolayer, multilayer to bulk material. *Chem. Soc. Rev.* **44**, 2757–2785 (2015).
- Mak, K. F., Lee, C., Hone, C., Shan, J. & Heinz, T. F. Atomically thin MoS₂: a new direct-gap semiconductor. *Phys. Rev. Lett.* **105**, 136805 (2010).
- Splendiani, A. et al. Emerging photoluminescence in monolayer MoS₂. *Nano Lett.* **10**, 1271–1275 (2010).
- Radisavljevic, B., Radenovic, A., Brivio, J., Giacometti, V. & Kis, A. Single-layer MoS₂ transistors. *Nat. Nanotechnol.* **6**, 147–150 (2011).
- Doratotaj, D., Simpson, J. R. & Yan, J.-A. Probing the uniaxial strains in MoS₂ using polarized Raman spectroscopy: a first-principles study. *Phys. Rev. B* **93**, 075401 (2016).
- Friemelt, K., Lux-Steiner, M.-C. & Bucher, E. Optical properties of the layered transition-metal-dichalcogenide ReS₂: anisotropy in the van der Waals plane. *J. Appl. Phys.* **74**, 5266 (1993).
- Camellini, A. et al. Optical characterization of anisotropic MoS₂ nanosheets. 2017 European Conference on Lasers and Electro-Optics and European Quantum Electronics Conference EIP2 (2017).
- Nam, G.-H. et al. In-plane anisotropic properties of 1T'-MoS₂ layers. *Adv. Mater.* **31**, 1807764 (2019).
- Wei, G., Lenferink, E. J., Czaplowski, D. A. & Stern, N. P. Width-dependent photoluminescence and anisotropic Raman spectroscopy from monolayer MoS₂ nanoribbons. Preprint at <https://arxiv.org/abs/1709.04001> (2017).
- LaMountain, T., Lenferink, E. J., Chen, Y.-J., Stanev, T. K. & Stern, N. P. Environmental engineering of transition metal dichalcogenide optoelectronics. *Front. of Phys.* **13**, 138114 (2018).
- Molina-Sánchez, A., Hummer, K. & Wirtz, L. Vibrational and optical properties of MoS₂: from monolayer to bulk. *Surf. Sci. Rep.* **70**, 554–586 (2015).
- Cheng, R. et al. Electroluminescence and photocurrent generation from atomically sharp WSe₂/MoS₂ heterojunction p-n diodes. *Nano Lett.* **14**, 5590–5597 (2014).
- Xia, F., Wang, H., Xiao, D. & Ramasubramaniam, M. A. Two-dimensional material nanophotonics. *Nat. Photon.* **8**, 899–907 (2014).
- Baugher, B. W. H., Churchill, H. O. H., Yang, Y. & Jarillo-Herrero, P. Intrinsic electronic transport properties of high quality monolayer and bilayer MoS₂. *Nano Lett.* **13**, 4212–4216 (2013).
- Rice, C., Young, R. J., Zan, R. & Bangert, U. Raman-scattering measurements and first-principles calculations of strain-induced phonon shifts in monolayer MoS₂. *Phys. Rev. B* **87**, 081307(R) (2013).
- Qiu, D. Y., daJornada, F. H. & Louie, S. G. Optical spectrum of MoS₂: Many-body effects and diversity of exciton states. *Phys. Rev. Lett.* **111**, 216805 (2013).

28. Xiao, D., Liu, G.-B., Feng, W., Xu, X. & Yao, W. Coupled spin and valley physics in monolayers of MoS₂ and other group-VI dichalcogenides. *Phys. Rev. Lett.* **108**, 196802 (2012).
29. Mak, K. F., McGill, K. L., Park, J. & McEuen, P. L. The valley Hall effect in MoS₂ transistors. *Science* **344**, 1489–1492 (2014).
30. Wang, Q. H., Kalantar-Zadeh, K., Kis, A., Coleman, J. N. & Strano, M. S. Electronics and optoelectronics of two-dimensional transition metal dichalcogenides. *Nat. Nanotechnol.* **7**, 699–712 (2012).
31. Lopez-Sanchez, O., Lembke, D., Kayci, M., Radenovic, A. & Kis, A. Ultrasensitive photodetectors based on monolayer MoS₂. *Nat. Nanotechnol.* **8**, 497–501 (2013).
32. Wang, Y., Cong, C., Qiu, C. & Yu, T. Raman spectroscopy study of lattice vibration and crystallographic orientation of monolayer MoS₂. *Small* **9**, 2857–2861 (2013).
33. Saito, R., Tatsumi, Y., Huang, S., Ling, X. & Dresselhaus, M. S. Raman spectroscopy of transition metal dichalcogenides. *J. Phys. Cond. Mater.* **28**, 353002 (2016).
34. Lee, C. et al. Anomalous lattice vibrations of single- and few-layer MoS₂. *ACS Nano* **4**, 2695–2700 (2010).
35. Li, H. et al. From bulk to monolayer MoS₂: evolution of Raman scattering. *Adv. Funct. Mater.* **22**, 1385–1390 (2012).
36. Huang, S. et al. Probing the interlayer coupling of twisted bilayer MoS₂ using photoluminescence spectroscopy. *Nano Lett.* **14**, 5500–5508 (2014).
37. Ji, J. et al. Giant magneto-optical Raman effect in a layered transition metal compound. *Proc. Natl. Acad. Sci. USA* **113**, 2349–2353 (2016).
38. Parkin, W. M. et al. Raman shifts in electron-irradiated monolayer MoS₂. *ACS Nano* **10**, 4134–4142 (2016).
39. Kravets, V. G., Fan, W., Wu, G. H. A., Yu, T., Imaizumi, S. & Grigorenko, A. N. Measurements of electrically tunable refractive index of MoS₂ monolayer and its usage in optical modulators. *npj 2D Mater. Appl.* **3**, 36 (2019).
40. Ghosh, T., Bardhan, M., Bhattacharya, M. & Satpati, B. Study of inelastic mean free path of metal nanostructures using energy filtered transmission electron microscopy imaging. *J. Microscopy* **258**, 253–258 (2015).
41. Iakoubovskii, K., Mitsuishi, K., Nakayama, Y. & Furuya, K. Mean free path of inelastic electron scattering in elemental solids and oxides using transmission electron microscopy: atomic number dependent oscillatory behavior. *Phys. Rev. B* **77**, 104102 (2008).
42. Miao, H. et al. Hydrothermal synthesis of MoS₂ nanosheets films: microstructure and formation mechanism research. *Mater. Lett.* **166**, 121–124 (2016).
43. Guo, J., Zhu, H., Sun, Y., Tanga, L. & Zhang, X. Boosting the lithium storage performance of MoS₂ with graphene quantum dots. *J. Mater. Chem. A* **4**, 4783–4789 (2016).
44. Rietveld, H. M. A profile refinement method for nuclear and magnetic structures. *J. Appl. Cryst.* **2**, 65–71 (1969).
45. Lutterotti, L. MAUD Version 1.85 (2002).
46. Borsella, E. et al. MoS₂ nanoparticles produced by laser induced synthesis from gaseous precursors. *J. Mat. Sc. Lett.* **20**, 187–191 (2001).
47. Gong, L. et al. Emergence of photoluminescence on bulk MoS₂ by laser thinning and gold particle decoration. *Nano Res.* **11**, 4574–4586 (2018).
48. Ye, M., Winslow, D., Zhang, D., Pandey, R. & Yap, Y. Recent advancement on the optical properties of two-dimensional molybdenum disulfide (MoS₂) thin films. *Photonics* **2**, 288 (2015).
49. Chakraborty, B., Matte, H. S. S. R., Sood, A. K. & Rao, C. N. R. Layer-dependent resonant Raman scattering of a few layer MoS₂. *J. Raman Spectrosc.* **44**, 92–96 (2013).
50. Sahoo, S., Gaur, A. P. S., Ahmadi, M., Guinel, M. J.-F. & Katiyar, R. S. Temperature-dependent Raman studies and thermal conductivity of few-layer MoS₂. *J. Phys. Chem. C* **117**, 9042–9047 (2013).
51. Wu, W. et al. Piezoelectricity of single-atomic-layer MoS₂ for energy conversion and piezotronics. *Nature* **514**, 470 (2014).
52. Zhu, H. et al. Observation of piezoelectricity in free-standing monolayer MoS₂. *Nat. Nanotechnol.* **10**, 151–155 (2015).
53. Zhou, K.-G. et al. Raman modes of MoS₂ used as fingerprint of van der Waals interactions in 2-D crystal-based heterostructures. *ACS Nano* **8**, 9914–9924 (2014).
54. Mitra, S. et al. Magnetodielectric effect in graphene-PVA nanocomposites. *J. Phys. Chem. C* **115**, 14285–14289 (2011).
55. Giannozzi, P. et al. Advanced capabilities for materials modelling with quantum ESPRESSO. *J. Phys.: Cond. Mater.* **29**, 465901 (2017).
56. Giannozzi, P. et al. QUANTUM ESPRESSO: a modular and open-source software project for quantum simulations of materials. *J. Phys.: Cond. Mater.* **21**, 395502 (2009).
57. Perdew, J. P. et al. Restoring the density-gradient expansion for exchange in solids and surfaces. *Phys. Rev. Lett.* **100**, 136406 (2008).
58. Wakabayashi, N., Smith, H. G. & Nicklow, R. M. Lattice dynamics of hexagonal MoS₂ studied by neutron scattering. *Phys. Rev. B* **12**, 659 (1975).
59. He, L. et al. Accuracy of generalized gradient approximation functionals for density-functional perturbation theory calculations. *Phys. Rev. B* **89**, 064305 (2014).
60. Grimme, S., Antony, J., Ehrlich, S. & Krieg, H. A consistent and accurate ab initio parametrization of density functional dispersion correction (DFT-D) for the 94 elements H-Pu. *J. Chem. Phys.* **132**, 154104 (2010).

ACKNOWLEDGEMENTS

The authors thank Prabir Pal of NPL, New Delhi for help in device fabrication. D.S. would like to acknowledge DST, India for INSPIRE faculty award (No. DST/INSPIRE/04/2015/000579) and CSC—the Finnish IT Center for Science for computational resources. The authors, S.M. and A.S. thank the Director of Bose Institute, Kolkata, India for the moral and financial support for this work.

AUTHOR CONTRIBUTIONS

S.M. and A.S. designed and directed the project. S.S.S. prepared the sample. S.M. and S.S.S. performed the Raman spectroscopy experiments. S.M. analyzed the data and prepared the figures. D.S. performed the DFT calculations and analysis thereof with input from S.M., M.K. and A.S. S.D. performed the crystal structure analysis. B.S. performed the transmission electron microscopy on the sample. A.G. and M.K. contributed intellectually to the project. S.M. wrote the paper with input from all the authors. A.S. supervised the project. All the authors have gone through the paper and commented on it.

COMPETING INTERESTS

The authors declare no competing interests.

ADDITIONAL INFORMATION

Supplementary information is available for this paper at <https://doi.org/10.1038/s41699-020-0138-y>.

Correspondence and requests for materials should be addressed to S.M. or A.S.

Reprints and permission information is available at <http://www.nature.com/reprints>

Publisher's note Springer Nature remains neutral with regard to jurisdictional claims in published maps and institutional affiliations.



Open Access This article is licensed under a Creative Commons Attribution 4.0 International License, which permits use, sharing, adaptation, distribution and reproduction in any medium or format, as long as you give appropriate credit to the original author(s) and the source, provide a link to the Creative Commons license, and indicate if changes were made. The images or other third party material in this article are included in the article's Creative Commons license, unless indicated otherwise in a credit line to the material. If material is not included in the article's Creative Commons license and your intended use is not permitted by statutory regulation or exceeds the permitted use, you will need to obtain permission directly from the copyright holder. To view a copy of this license, visit <http://creativecommons.org/licenses/by/4.0/>.

© The Author(s) 2020